

1 **Tropopause Evolution in a Rapidly Intensifying Tropical Cyclone: A Static**
2 **Stability Budget Analysis**

3 Patrick Duran* and John Molinari

4 *University at Albany, State University of New York, Albany, NY*

5 **Corresponding author address:* Department of Atmospheric and Environmental Sciences, Univer-
6 sity at Albany, State University of New York, 1400 Washington Avenue, Albany, NY.

7 E-mail: pduran2008@gmail.com

ABSTRACT

⁸ We have some cool results!

9 **1. Introduction**

10 There will be a whole bunch of papers cited here...

11 **2. Model Setup**

12 The numerical simulations were performed using version 19.4 of Cloud Model
13 1 (CM1) described in Bryan and Rotunno (2009) and available online at
14 <http://www2.mmm.ucar.edu/people/bryan/cm1/>. The fully-compressible equations of mo-
15 tion were integrated on a 3000-km-wide, 35-km-deep, axisymmetric grid with 1-km horizontal
16 and 250-m vertical grid spacing. Horizontal turbulence was parameterized using a Smagorinsky
17 scheme described in Bryan and Rotunno (2009, their Eq. 17), with a prescribed mixing length
18 that varied linearly from 100 m at a surface pressure of 1015 hPa to 1000 m at a surface pressure
19 of 900 hPa. This formulation allows for realistically-large horizontal mixing lengths near the
20 hurricane’s inner core, consistent with the results of Bryan (2012), while not over-representing
21 horizontal turbulence in convection at outer radii. Vertical turbulence was parameterized using
22 the formulation of Markowski and Bryan (2016, their Eq. 6), using an asymptotic vertical
23 mixing length of 100 m. A Rayleigh damping layer was applied outside of the 2900-km radius
24 and above the 25-km level to prevent spurious gravity wave reflection at the model boundaries.
25 Microphysical processes were parameterized using the Thompson et al. (2004) microphysics
26 scheme and radiative heating tendencies were computed every two minutes using the RRTMG
27 longwave and shortwave schemes (Iacono et al. 2008). A horizontally-homogeneous temperature
28 and humidity field was initialized with a mean sounding computed using all dropsondes deployed
29 during the TCI flight conducted within and around Tropical Storm Patricia on 21 October, 2015
30 (see Doyle et al. 2017 for details.) Above 19 km, where few TCI observations were available, the
31 temperature profile was assumed to be isothermal. Since relative humidity measurements were

unreliable at temperatures below -40°C (Bell et al. 2016), the water vapor mixing ratio was set to zero above 16 km. The vortex described in Rotunno and Emanuel (1987, their Eq. 37) was used to initialize the wind field, setting all parameters equal to the values used therein.

3. Budget Computation

The static stability can be expressed as the squared Brunt Väisälä frequency:

$$N^2 = \frac{g}{\theta_v} \frac{\partial \theta_v}{\partial z} \quad (1)$$

In the tropopause layer, q_s , $\frac{\partial q_s}{\partial T}$, and $\frac{\partial q_t}{\partial z}$ approach zero; thus, Eq. 1 reduces to:

$$N^2 = \frac{g}{\theta_v} \frac{\partial \theta_v}{\partial z}, \quad (2)$$

where g is gravitational acceleration and θ_v is the virtual potential temperature. To compute N^2 , CM1 uses Eq. 1 in saturated environments and Eq. 2 in unsaturated environments. For mathematical simplicity, only Eq. 2 will be used for the budget computations herein¹. Taking the time derivative of Eq.2 yields the static stability tendency:

4. Results

Put description of Fig. 1 in this section.

Don't forget to mention 1-2-1 smoother.

a. Static stability evolution

The average N^2 over the first day of the simulation (Fig. 2a) indicates the presence of a static stability maximum about 400 m above the cold-point tropopause. This lower-stratospheric stable layer had begun to erode during the initial spin-up period, with the maximum destabilization

¹The validity of this approximation will be substantiated later in this section.

occurring at the innermost radii. This decrease in static stability continued into the second day of the simulation (Fig. 2b) as the storm intensified to hurricane strength (Fig. 1). Destabilization was particularly pronounced over the developing eye, where the time-mean cold-point tropopause height increased by up to 400 m compared to the previous day. Over the developing eyewall and outer rainband regions, meanwhile, the tropopause height remained nearly constant. During the third day of the simulation (Fig. 2c), static stability over the eye continued to decrease, and the cold-point tropopause height rose to 18.3 km at the storm center. The tropopause sloped sharply downward over the innermost radii, reaching the 16.4-km level near the 50-km radius. This local minimum in tropopause height corresponded to the eyewall region, where upper-tropospheric static stability increased during this time period. Outside of the eyewall region, static stability began to increase in the layer immediately overlying the cold-point tropopause. This stable layer sloped upward with radius, which corresponded to an upward-sloping tropopause radially outside of the eyewall region. Over the next 24 hours (Fig. 2d), as the storm's maximum 10-m wind speed leveled off near 80 m s^{-1} (Fig. 1), the upper-tropospheric static stability within the eyewall region continued to strengthen, as did the static stability just above the cold-point tropopause radially outside of the eyewall. As the stable layer strengthened, its altitude rose slightly, which corresponded to a slight increase in tropopause height outside of the eyewall during this period. Within the upper troposphere radially outside of the eyewall, meanwhile, static stability decreased such that it was nearly neutral in a thin layer between the 120- and 150-km radii. The eye region likewise continued to destabilize, and the cold-point tropopause height increased to a level above 18.5 km. This static stability evolution closely follows that observed in Hurricane Patricia (2015; Duran and Molinari 2018).

71 *b. Static stability budget analysis*

72 The left column of Fig. 3 depicts 24-hour changes in N^2 over each of the four days of the
73 simulation. These represent bulk changes computed by subtracting the instantaneous N^2 at the
74 initial time from the instantaneous N^2 at the final time. The middle column of Fig. 3 represents
75 the change in N^2 computed using Eq. XXX and the method described in Section 3. The residual
76 between these two computations (Fig. 3, right column) is much smaller than the change in N^2 ,
77 meaning that the budget performs well within the analysis domain.

78 To determine which of the budget terms are most important, a time series of the contribution of
79 each of the budget terms in Eq. XXX to the tropopause-layer static stability tendency is plotted
80 in Fig. 4. For this figure, each of the budget terms is computed using the method described in
81 Section 3, except with 1-hour averaging intervals instead of 24-hour intervals. The absolute values
82 of these tendencies are then averaged over the radius-height domain depicted in Fig. 3 and plotted
83 as a time series². Advection (Fig. 4, red line) plays an important role in the mean tropopause-
84 layer static stability tendency at all times, and vertical turbulence (Fig. 4, blue line) and radiation
85 (Fig. 4, dark green line) both become important after 48 hours. Although the contribution from
86 horizontal turbulence (Fig. 4, purple line) becomes more important after 72 hours, it is confined
87 to a very small region immediately surrounding the eyewall tangential velocity maximum (not
88 shown), and is negligible throughout the rest of the tropopause layer. The remaining two processes
89 - microphysics and dissipative heating (Fig. 4, orange and light green lines, respectively) - lie atop
90 one another near zero. These time series indicate that, at all times, three budget terms dominate the
91 tropopause-layer static stability tendency: advection, vertical turbulence, and radiation. Variations

²It will be seen in subsequent figures that each of the terms contributes both positively and negatively to the N^2 tendency within the analysis domain. Thus, taking an average over the domain tends to wash out the positive and negative contributions. To circumvent this problem, the absolute value of each of the terms is averaged, yielding a time series of the mean magnitude of each budget term.

in the magnitude and spatial structure of these terms drive the static stability changes depicted in Fig. 2; subsequent sections will focus on these variations and what causes them.

(i) 0-24 hours The first 24 hours of the simulation was characterized by a weakening of the lower-stratospheric static stability maximum above 17 km (Fig. ??a, purple shading) and an increase in static stability below (green shading). Although these tendencies extended out to the 200-km radius, they were particularly pronounced at innermost radii. A comparison of the contributions of advection (Fig. ??b), vertical turbulence (Fig. ??c), and radiation (Fig. ??d) reveals that advection is primarily responsible for the change in static stability during this period. ...Explain this in the context of radial and vertical velocities...

(ii) 24-48 hours During the second day of the simulation, the lower-stratospheric stable layer continued to weaken (Fig. 6a). This weakening trend in the 16.75-17.75-km layer extended from the 50 km radius outward to past 200 km, and was primarily driven by advection (Fig. 6b). Below this layer, static stability began to increase slightly. This stabilization had contributions from both vertical turbulence (Fig. 6c) and radiation (Fig. 6d) in the 16-16.5-km layer. ...Explain this in context of mean vertical mixing coefficient and mean radiative heating tendency... Meanwhile, radially inward of 60 km, static stability below 17.5 km continued to weaken, primarily due to advective processes.

(iii) 48-72 hours The third day of the simulation marked a dramatic change in the structure of the tropopause-layer static stability tendencies. During this time, static stability increased markedly in an upward-sloping region within the 30-60-km radial band (Fig. 7a), and also increased within the 16.75-17.5-km layer out to at least the 200-km radius. As this layer stabilized, the layer immediately below it destabilized in a broad region extending from 60-200 km. Examination of the contribution from total advection (Fig. 7b) reveals that advection no longer dominates the

static stability tendencies. Instead, a combination of vertical turbulence (Fig. 7c) and radiation (Fig. 7d) overcomes the destabilizing influence of advection to create the layer of increasing static stability. Meanwhile, the destabilizing influence of vertical turbulence in a broad region below 17 km combines with a small region of destabilization due to radiation in the 50-120-km radial band combine to destabilize the layer below 16.5 km in the 50-200-km radial band. Comparing the sum of advection and vertical turbulence (Fig. 7e) to the sum of advection, vertical turbulence, and radiation (Fig. 7f) reveals that radiation plays a fundamental role in the re-strengthening of the lower-stratospheric stable layer during this time.

(iv) 72-96 hours

Acknowledgments. Jeff Kepert and Rob Fovell.

References

- Bell, M. M., and Coauthors, 2016: Office of Naval Research Tropical Cyclone Intensity (TCI) 2015 NASA WB-57 High Density Dropsonde Sounding System (HDSS) data, version 1.0. doi: 10.5065/D6KW5D8M.
- Bryan, G. H., 2012: Effects of surface exchange coefficients and turbulence length scales on the intensity and structure of numerically simulated hurricanes. *Mon. Wea. Rev.*, **140**, 1125–1143.
- Bryan, G. H., and R. Rotunno, 2009: The maximum intensity of tropical cyclones in axisymmetric numerical model simulations. *Mon. Wea. Rev.*, **137**, 1770–1789.
- Doyle, J. D., and Coauthors, 2017: A view of tropical cyclones from above: The Tropical Cyclone Intensity (TCI) Experiment. *Bull. Amer. Meteor. Soc.*, **98**, 2113–2134.
- Duran, P., and J. Molinari, 2018: Dramatic inner-core tropopause variability during the rapid intensification of Hurricane Patricia (2015). *Mon. Wea. Rev.*, **XXX**, XXX–XXX.

137 Iacono, M. J., J. S. Delamere, E. J. Mlawer, M. W. Shephard, S. A. Clough, and W. D. Collins,
138 2008: Radiative forcing by long-lived greenhouse gases: Calculations with the AER radiative
139 transfer models. *J. Geophys. Res.*, **113** (D13103).

140 Markowski, P. M., and G. H. Bryan, 2016: LES of laminar flow in the PBL: A potential problem
141 for convective storm simulations. *Mon. Wea. Rev.*, **144**, 1841–1850.

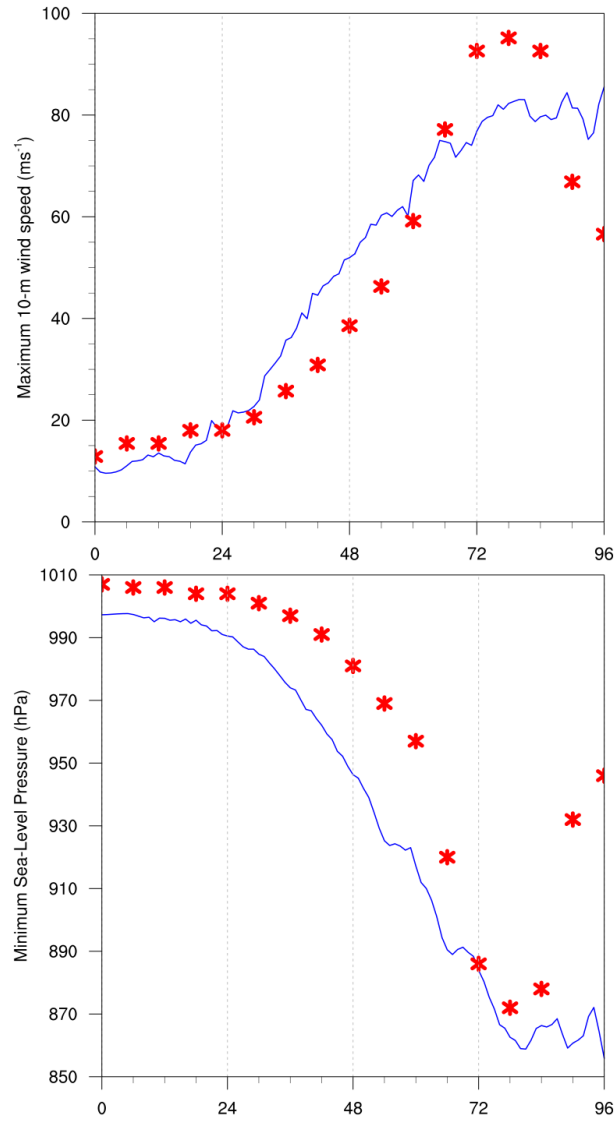
142 Rotunno, R., and K. A. Emanuel, 1987: An air-sea interaction theory for tropical cyclones. Part II:
143 Evolutionary study using a nonhydrostatic axisymmetric numerical model. *J. Atmos. Sci.*, **44**,
144 542–561.

145 Thompson, G., R. M. Rasmussen, and K. Manning, 2004: Explicit forecasts of winter precipitation
146 using an improved bulk microphysics scheme. Part I: Description and sensitivity analysis. *Mon.*
147 *Wea. Rev.*, **132**, 519–542.

LIST OF FIGURES

- Fig. 1.** The maximum 10-m wind speed (top panel; m s^{-2}) and minimum sea-level pressure (bottom panel; hPa) in the simulated storm (blue lines) and from Hurricane Patricia's best track (red stars). 12
- Fig. 2.** Twenty-four-hour averages of squared Brunt-Väisälä frequency (10^{-4} s^{-2}) over the first four days of the simulation. Orange lines represent the cold-point tropopause computed from the mean temperature field over the same time periods. 13
- Fig. 3.** Left panels: Twenty-four-hour changes in squared Brunt-Väisälä frequency (10^{-4} s^{-2}) over (a) 0-24 hours, (b) 24-48 hours, (c) 48-72 hours, (d) 72-96 hours. Middle Panels: The N^2 change over the same time periods computed using Eq. XXX. Right Panels: The budget residual over the same time periods, computed by subtracting the budget change (middle column) from the model change (left column). 14
- Fig. 4.** Time series of the contribution of each of the budget terms to the time tendency of the squared Brunt-Väisälä frequency (N^2 ; 10^{-4} s^{-2}). For each budget term, the absolute value of the N^2 tendency is averaged both temporally over 1-hour periods (using output every minute), and spatially within the radius-height domain depicted in Fig. 3. 15
- Fig. 5.** (a) Total change in N^2 over the 0-24-hour period ($10^{-4} \text{ s}^{-2} (24 \text{ hr})^{-1}$) and the contributions to that change from (b) the sum of horizontal and vertical advection, (c) vertical turbulence, and (d) the sum of longwave and shortwave radiation. 16
- Fig. 6.** As in Fig. 5, but for the 24-48-hour period. 17

168	Fig. 7.	(a) Total change in N^2 over the 48-72-hour period ($10^{-4} \text{ s}^{-2} (24 \text{ hr})^{-1}$) and the contributions	
169		to that change from (b) the sum of horizontal and vertical advection, (c) vertical turbulence,	
170		(d) the sum of longwave and shortwave radiation, (e) the sum of horizontal advection, ver-	
171		tical advection, and vertical turbulence, and (f) the sum of horizontal advection, vertical	
172		advection, vertical turbulence, and longwave and shortwave radiation.	18
173	Fig. 8.	As in Fig. 7, but for the 72-96-hour period.	19
174	Fig. 9.	Radial velocity (m s^{-1} ; filled contours), potential temperature (K; thick black contours), and	
175		cold point tropopause height (orange line) averaged over (a) 0-24 hours, (b) 24-48 hours, (c)	
176		48-72 hours, and (d) 72-96 hours.	20
177	Fig. 10.	Vertical velocity (cm s^{-1} ; filled contours), potential temperature (K; thick black contours),	
178		and cold point tropopause height (orange line) averaged over (a) 0-24 hours, (b) 24-48 hours,	
179		(c) 48-72 hours, and (d) 72-96 hours.	21
180	Fig. 11.	Total condensate mixing ratio (g kg^{-1}) and cold point tropopause height (orange line) aver-	
181		aged over (a) 0-24 hours, (b) 24-48 hours, (c) 48-72 hours, and (d) 72-96 hours.	22



182 FIG. 1. The maximum 10-m wind speed (top panel; m s^{-2}) and minimum sea-level pressure (bottom panel;
 183 hPa) in the simulated storm (blue lines) and from Hurricane Patricia's best track (red stars).

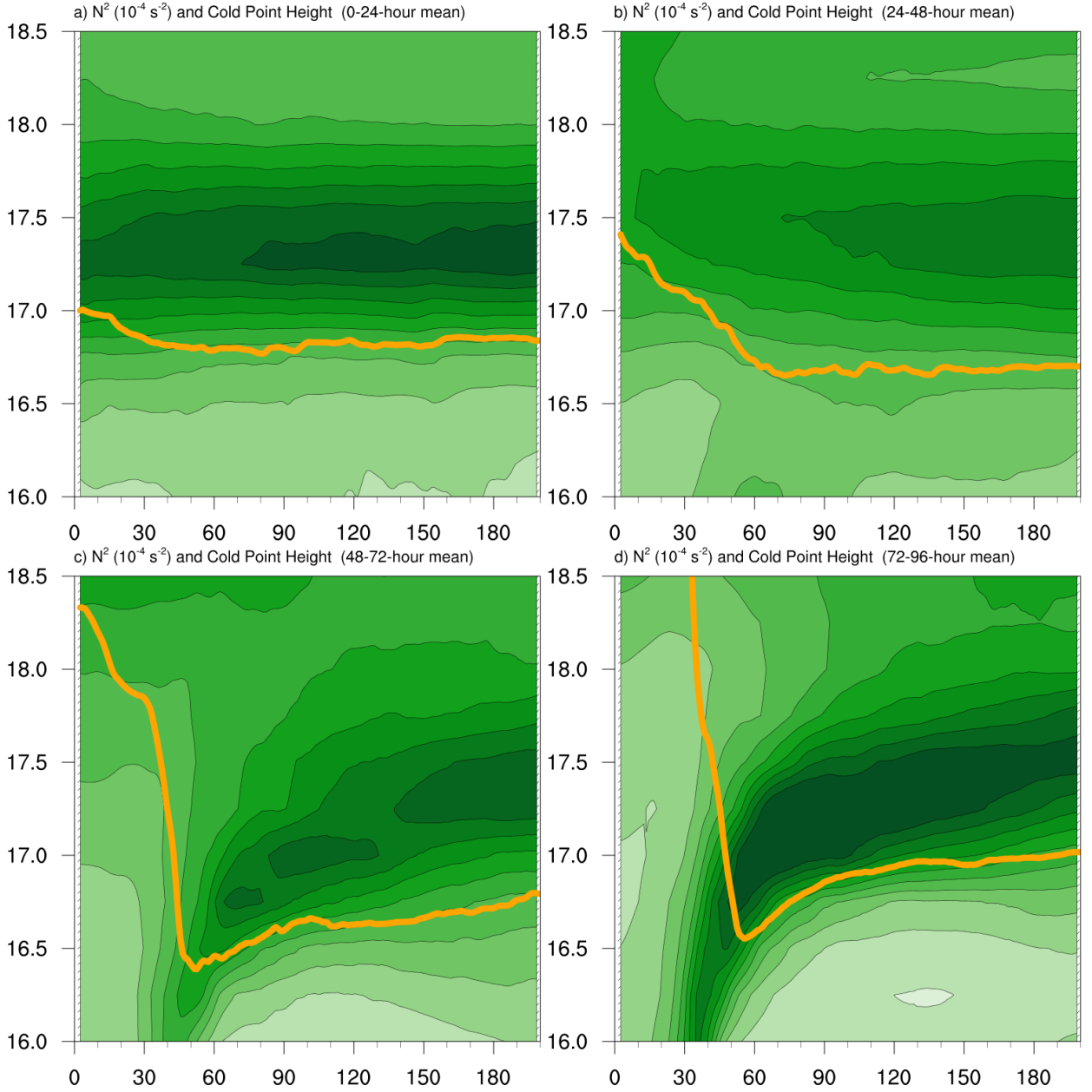
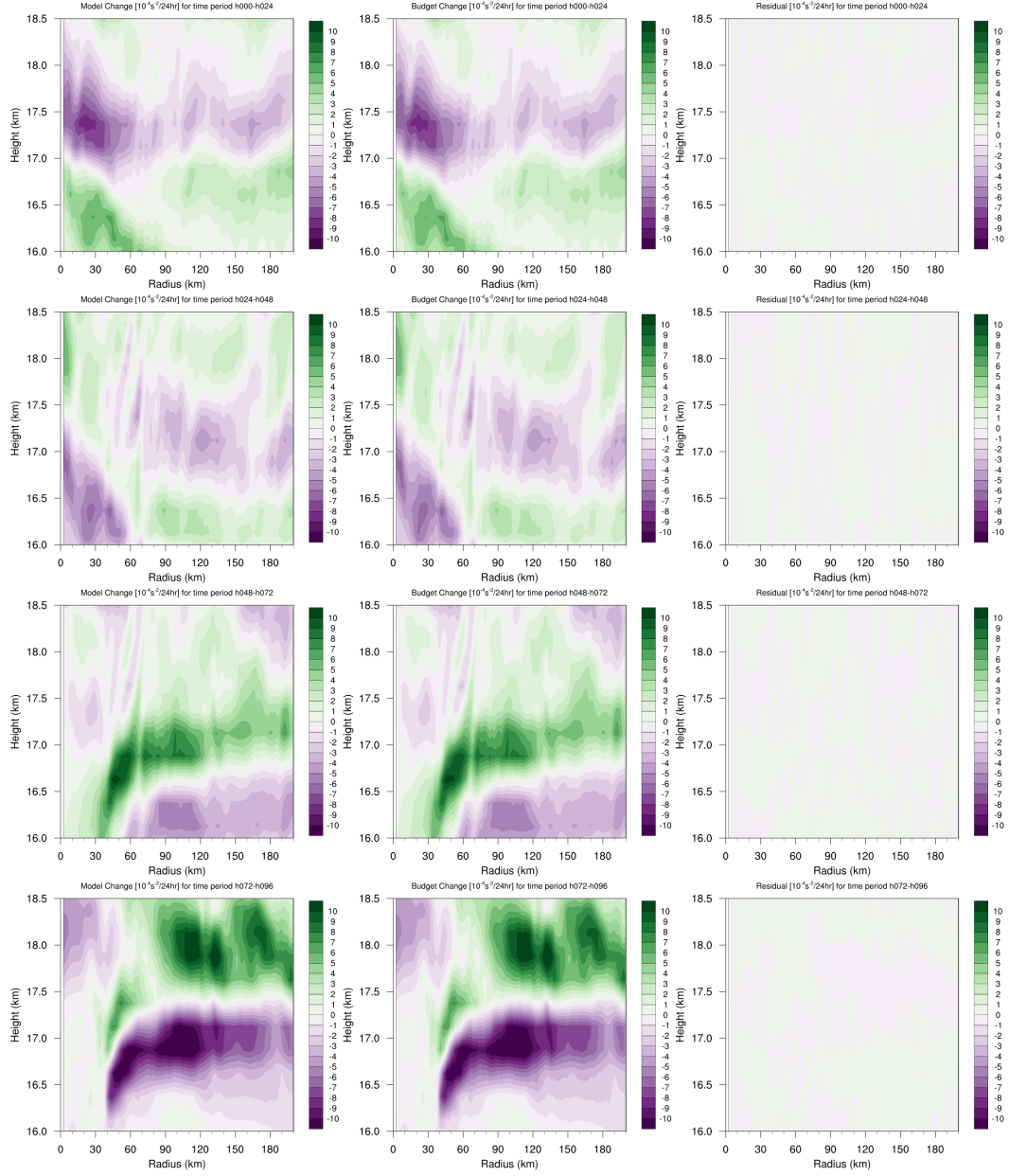


FIG. 2. Twenty-four-hour averages of squared Brunt-Väisälä frequency (10^{-4} s^{-2}) over the first four days of the simulation. Orange lines represent the cold-point tropopause computed from the mean temperature field over the same time periods.



187 FIG. 3. Left panels: Twenty-four-hour changes in squared Brunt-Väisälä frequency (10^{-4} s^{-2}) over (a) 0-24
 188 hours, (b) 24-48 hours, (c) 48-72 hours, (d) 72-96 hours. Middle Panels: The N^2 change over the same time
 189 periods computed using Eq. XXX. Right Panels: The budget residual over the same time periods, computed by
 190 subtracting the budget change (middle column) from the model change (left column).

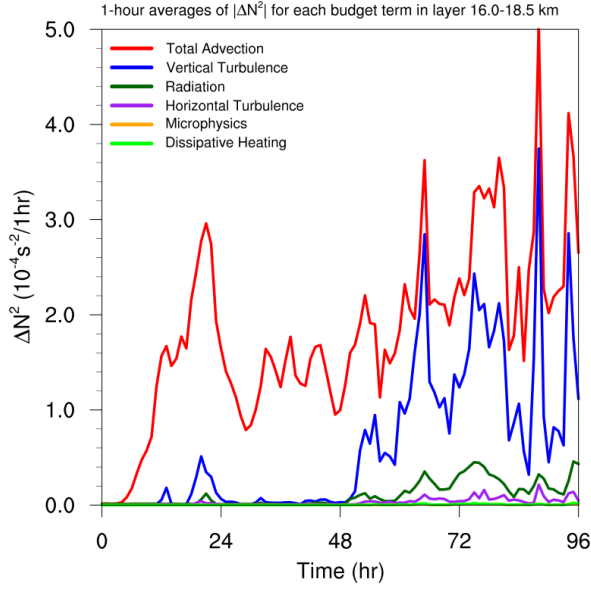


FIG. 4. Time series of the contribution of each of the budget terms to the time tendency of the squared Brunt-Väisälä frequency (N^2 ; 10^{-4} s^{-2}). For each budget term, the absolute value of the N^2 tendency is averaged both temporally over 1-hour periods (using output every minute), and spatially within the radius-height domain depicted in Fig. 3.

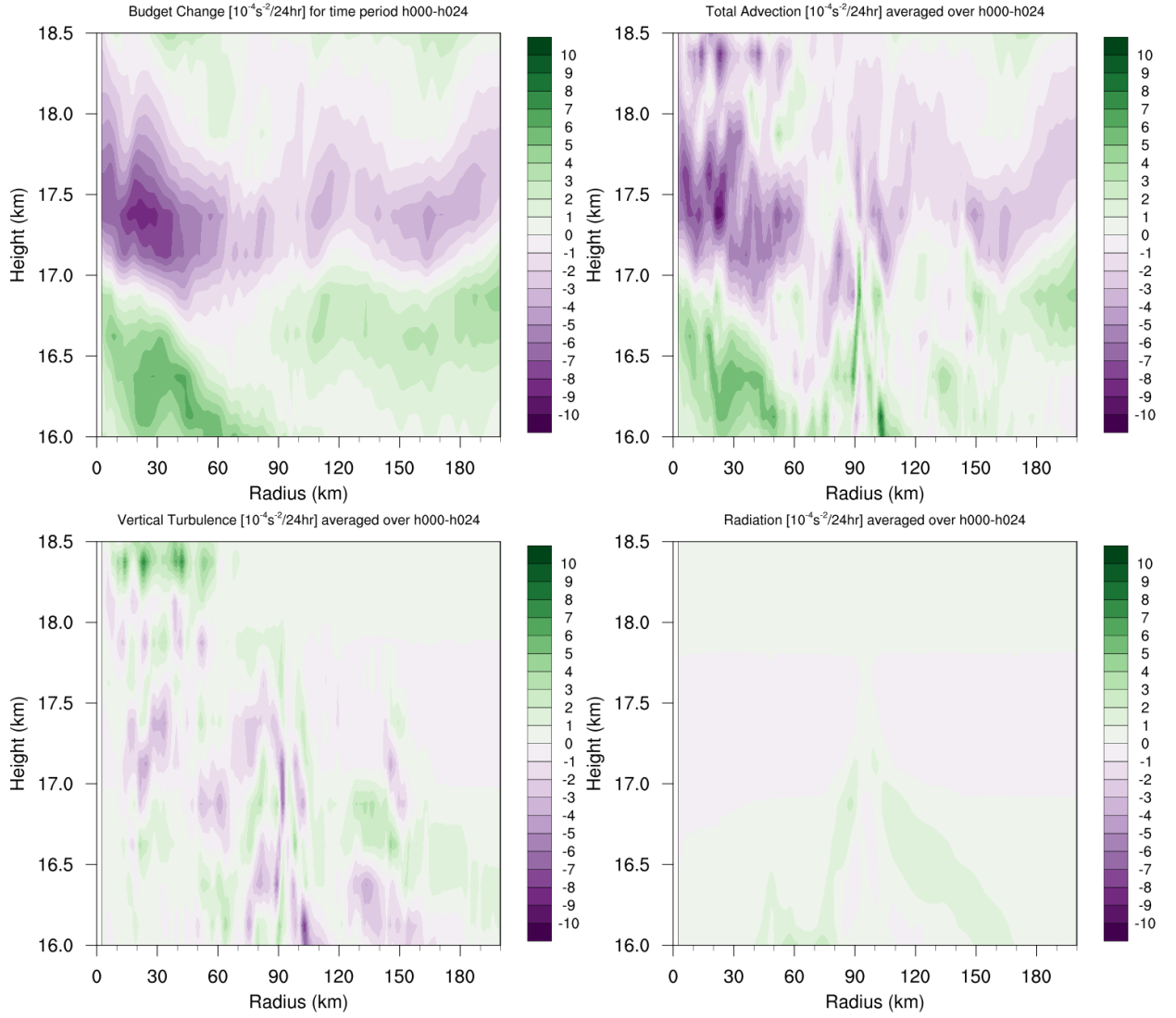


FIG. 5. (a) Total change in N^2 over the 0-24-hour period ($10^{-4} \text{ s}^{-2} (24 \text{ hr})^{-1}$) and the contributions to that change from (b) the sum of horizontal and vertical advection, (c) vertical turbulence, and (d) the sum of longwave and shortwave radiation.

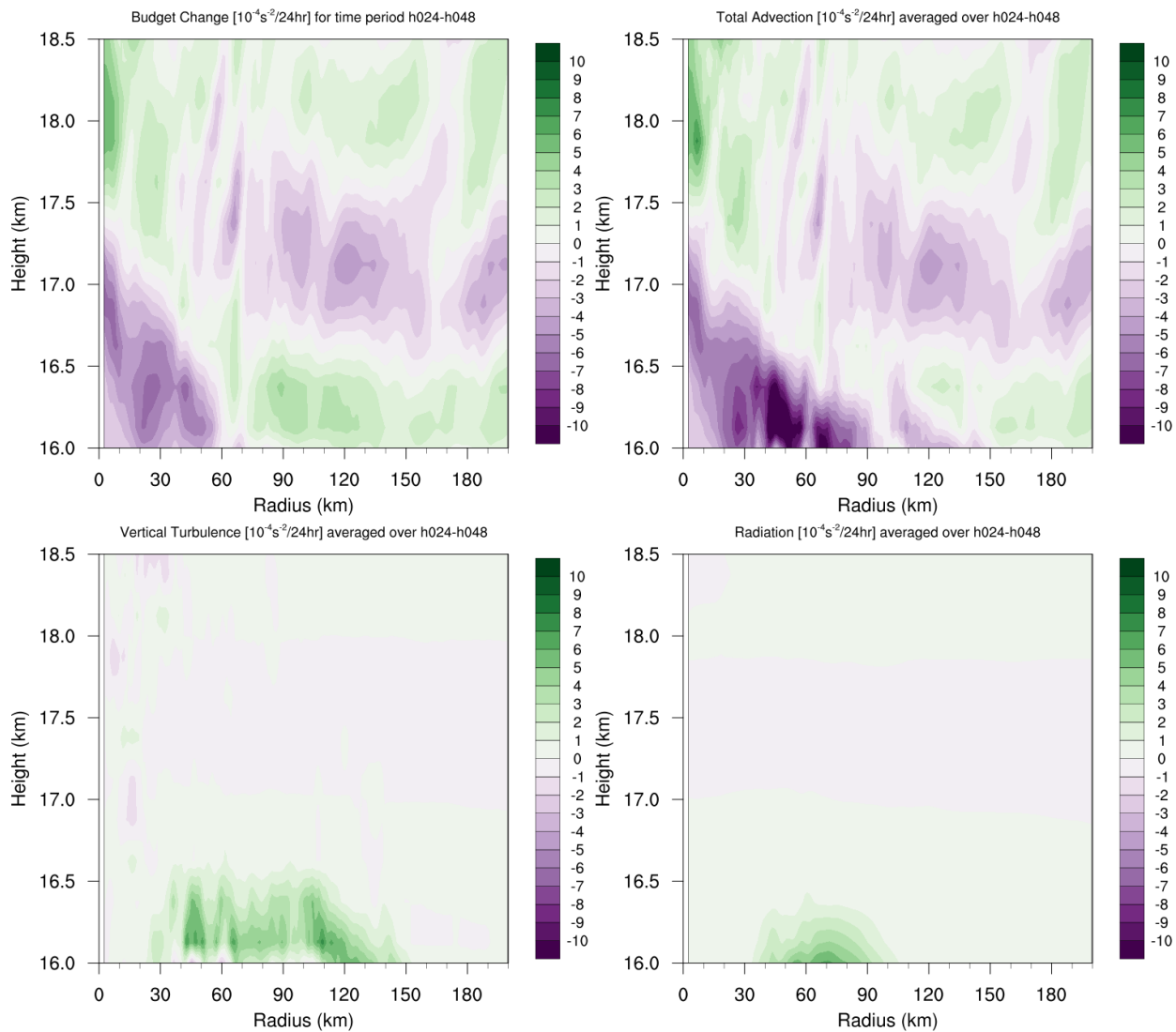


FIG. 6. As in Fig. 5, but for the 24-48-hour period.

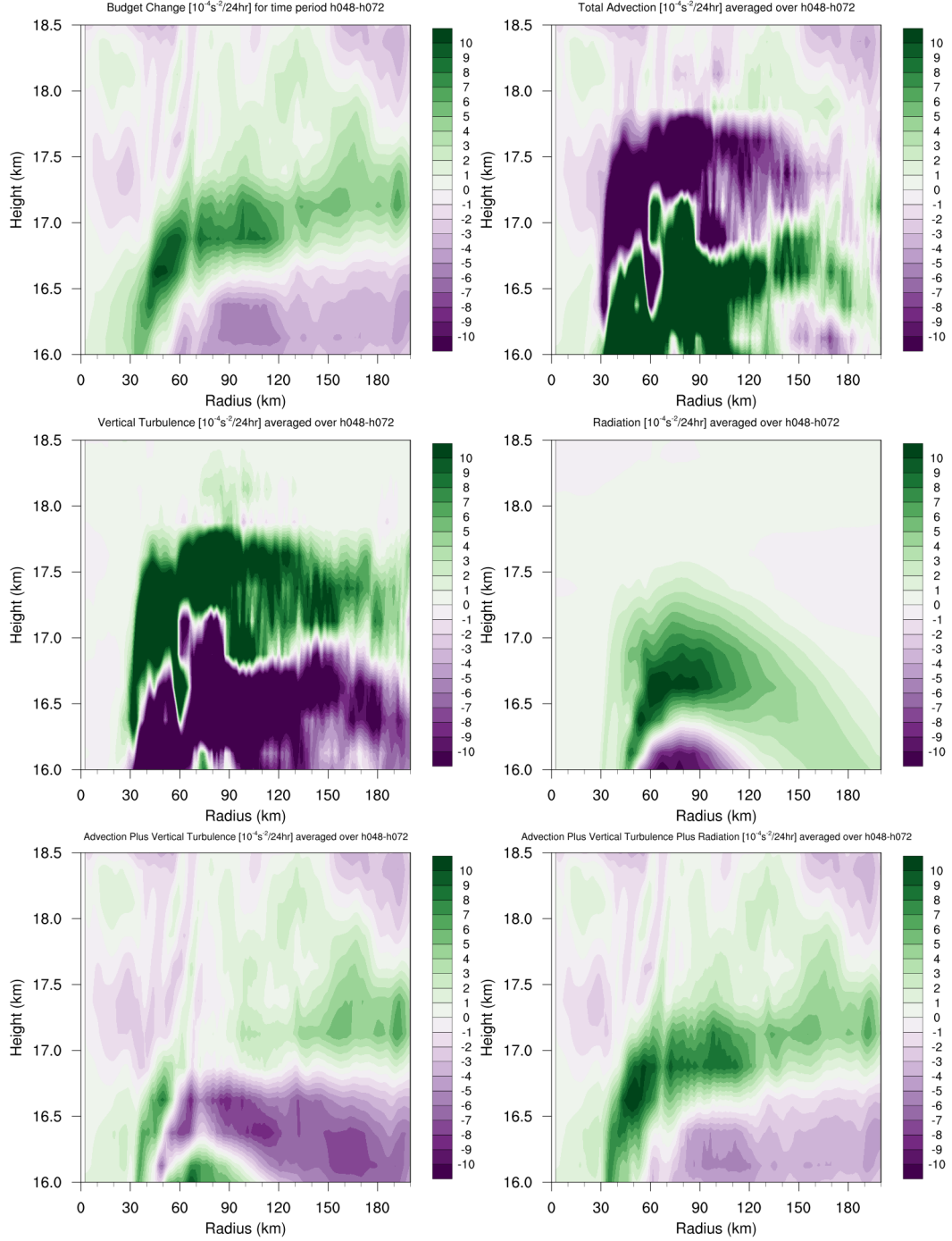


FIG. 7. (a) Total change in N^2 over the 48-72-hour period ($10^{-4} \text{ s}^{-2} (24 \text{ hr})^{-1}$) and the contributions to that change from (b) the sum of horizontal and vertical advection, (c) vertical turbulence, (d) the sum of longwave and shortwave radiation, (e) the sum of horizontal advection, vertical advection, and vertical turbulence, and (f) the sum of horizontal advection, vertical advection, vertical turbulence, and longwave and shortwave radiation.

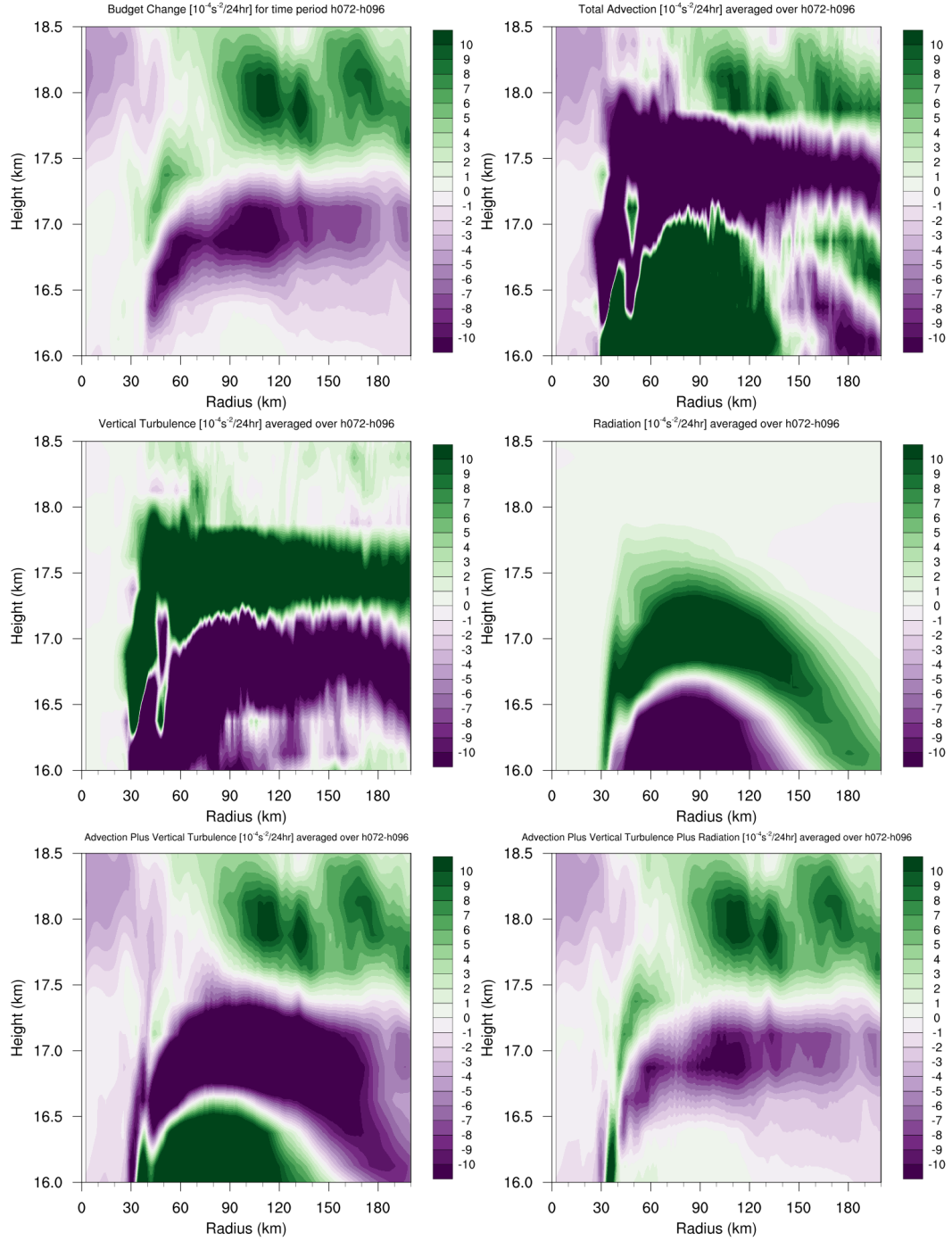


FIG. 8. As in Fig. 7, but for the 72-96-hour period.

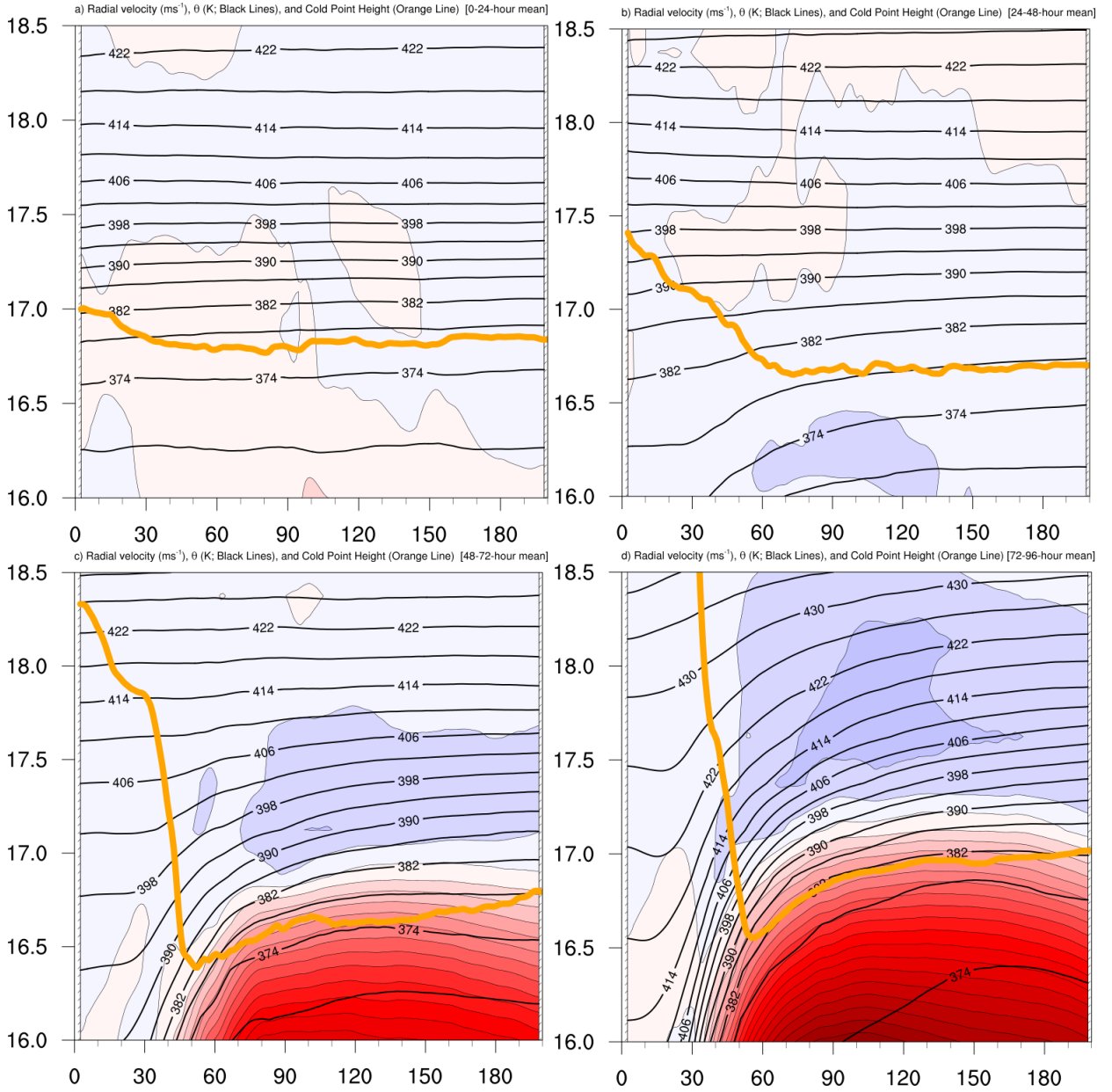


FIG. 9. Radial velocity (m s^{-1} ; filled contours), potential temperature (K; thick black contours), and cold point tropopause height (orange line) averaged over (a) 0-24 hours, (b) 24-48 hours, (c) 48-72 hours, and (d) 72-96 hours.

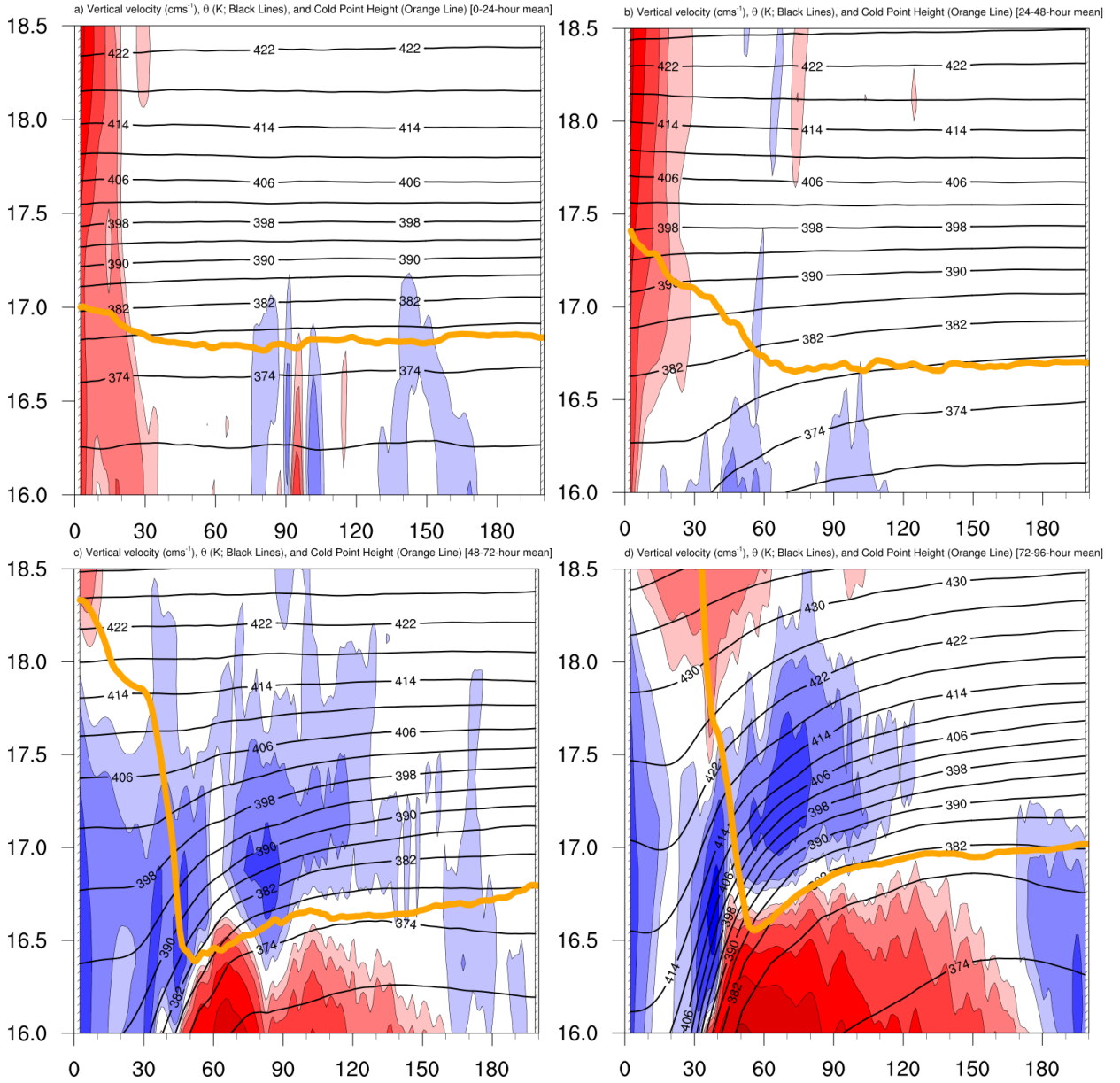


FIG. 10. Vertical velocity (cm s^{-1} ; filled contours), potential temperature (K ; thick black contours), and cold point tropopause height (orange line) averaged over (a) 0-24 hours, (b) 24-48 hours, (c) 48-72 hours, and (d) 72-96 hours.

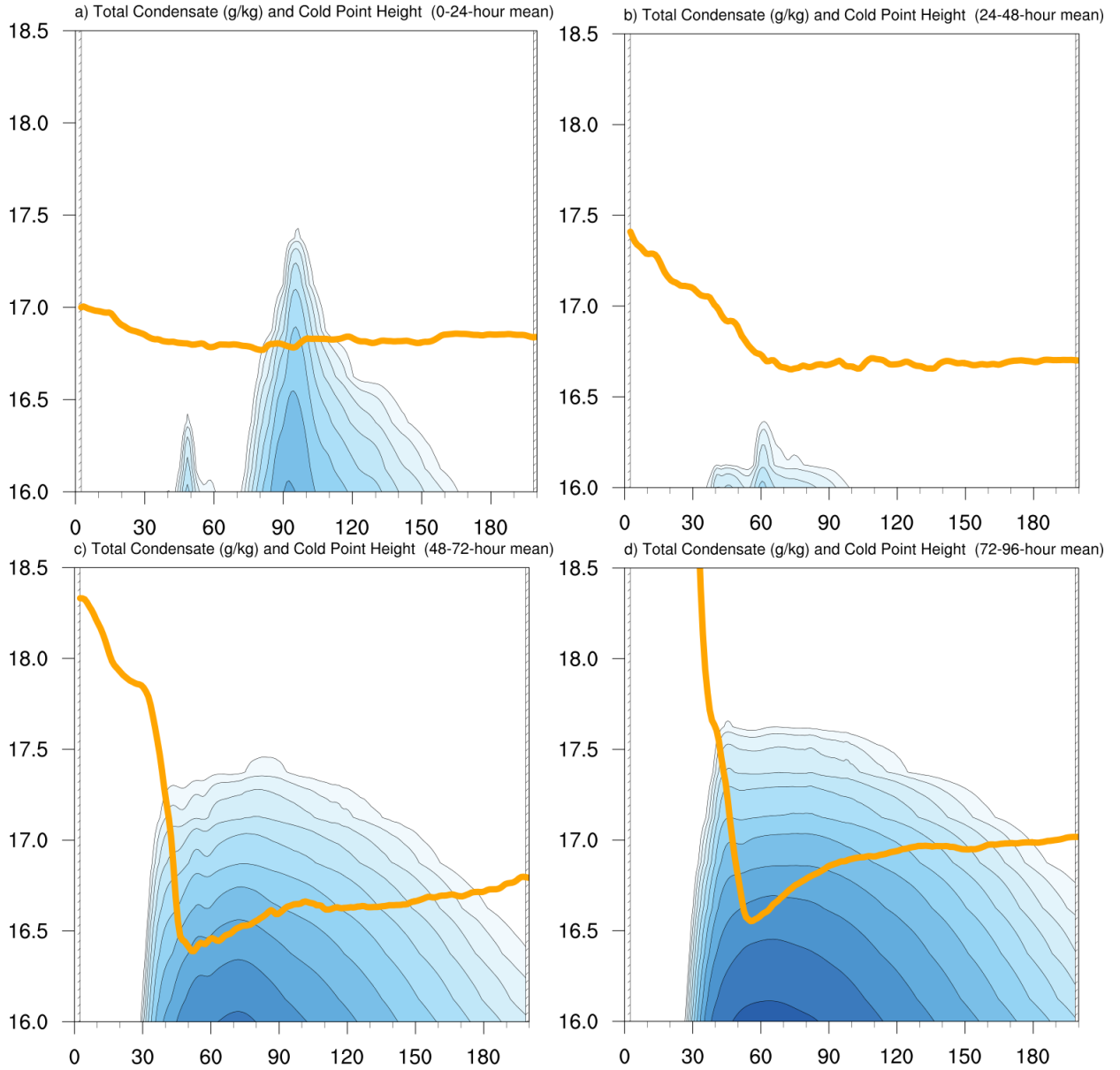


FIG. 11. Total condensate mixing ratio (g kg^{-1}) and cold point tropopause height (orange line) averaged over (a) 0-24 hours, (b) 24-48 hours, (c) 48-72 hours, and (d) 72-96 hours.